

# Framelet Representation of Tensor Nuclear Norm for Third-Order Tensor Completion

Tai-Xiang Jiang, Michael K. Ng, Xi-Le Zhao, and Ting-Zhu Huang

**Abstract**—The main aim of this paper is to develop a framelet representation of the tensor nuclear norm for third-order tensor completion. In the literature, the tensor nuclear norm can be computed by using tensor singular value decomposition based on the discrete Fourier transform matrix, and tensor completion can be performed by the minimization of the tensor nuclear norm which is the relaxation of the sum of matrix ranks from all Fourier transformed matrix frontal slices. These Fourier transformed matrix frontal slices are obtained by applying the discrete Fourier transform on the tubes of the original tensor. In this paper, we propose to employ the framelet representation of each tube so that a framelet transformed tensor can be constructed. Because of framelet basis redundancy, the representation of each tube is sparsely represented. When the matrix slices of the original tensor are highly correlated, we expect the corresponding sum of matrix ranks from all framelet transformed matrix frontal slices would be small, and the resulting tensor completion can be performed much better. The proposed minimization model is convex and global minimizers can be obtained. Numerical results on several types of multi-dimensional data (videos, multispectral images, and magnetic resonance imaging data) have tested and shown that the proposed method outperformed the other testing tensor completion methods.

**Index Terms**—Tensor completion, tensor nuclear norm, framelet, alternating direction method of multipliers

## I. INTRODUCTION

As a high order extension of matrix, the tensor is an important data format for multi-dimensional data applications, such as color image and video processing [1–4], hyperspectral data fusion [5, 6], personalized web search [7, 8], high-order web link analysis [9], magnetic resonance imaging (MRI) data recovery [10], and seismic data reconstruction [11]. Owing to the objective restrictions, for example, the imaging condition for the visual data acquiring and the limitation of the transmission bandwidth, the multi-dimensional data in many applications are incomplete. This motivates us to perform tensor completion, in which how to characterize and utilize

This work is supported by the National Natural Science Foundation of China (61772003, 61876203, and 61702083), HKRGC GRF (12306616, 12200317, 12300218, and 12300519), China Postdoctoral Science Foundation (2017M610628 and 2018T111031).

T.-X. Jiang is with the FinTech Innovation Center, the Financial Intelligence and Financial Engineering Research Key Laboratory of Sichuan province, School of Economic Information Engineering, Southwestern University of Finance and Economics, Chengdu, Sichuan, China (e-mail: taixiangjiang@gmail.com).

Michael K. Ng is with Department of Mathematics, The University of Hong Kong, Pokfulam, Hong Kong (e-mail: mng@maths.hku.hk).

X.-L. Zhao, and Ting-Zhu Huang are with the Research Center for Image and Vision Computing, School of Mathematical Sciences, University of Electronic Science and Technology of China, Chengdu 611731, P.R.China (e-mail: xlzhao122003@163.com; tingzhu Huang@126.com).

the internal structural information of these multidimensional data is of crucial importance.

For the matrix processing, low-rank models can effectively and efficiently handle two-dimensional data of various sources [12]. Generalized from matrix format, a tensor is able to contain more essentially structural information, being a powerful tool for dealing with multi-modal and multi-relational data [13]. Unfortunately, it is not easy to directly extend the low-rankness from the matrix to tensors. More precisely, there is not an exact (or unique) definition for the tensor’s rank. In the past decades, the most popular rank definitions are the CANDECOMP/PARAFAC (CP)-rank [14, 15] and the Tucker-rank [16, 17] (or denoted as “ $n$ -rank” in [18]). The CP-rank is based on the CP decomposition, however computing the CP-rank of a given tensor is NP-hard [19]. The Tucker rank is based on the Tucker decomposition, in which the tensor is unfolded along each mode unavoidably destroying the intrinsic structures of the tensor.

In this paper, we investigate the newly emerged tensor rank definitions, i.e., the tensor multi-rank and the tensor tubal-rank, which are computable and induced from the tensor singular value decomposition (t-SVD). The t-SVD is initially proposed by Braman *et al.* [20] and Kilmer *et al.* [21], based on the tensor-tensor product (denoted as t-prod), in which the third-order tensors are operated integrally avoiding the loss of information inherent in matricization or flattening of the tensor [22]. Meanwhile, the t-SVD has shown its superior performance in capturing the spatial-shifting correlation that is ubiquitous in real-world data [20, 21, 23]. Although the t-SVD is initially designed for third-order tensors, it has been extended to high order tensors with arbitrary dimensions [23, 24].

In [25], Kernfeld *et al.* note that the t-prod is based on a convolution-like operation, which can be implemented using the discrete Fourier transform (DFT). Then, given a third-order tensor  $\mathcal{X} \in \mathbb{R}^{n_1 \times n_2 \times n_3}$ , its Fourier transformed (along the third mode) tensor is denoted as  $\hat{\mathcal{X}} \in \mathbb{R}^{n_1 \times n_2 \times n_3}$  and its tensor multi-rank is a vector with the  $i$ -th element equal to the rank of  $i$ -th frontal slice of  $\hat{\mathcal{X}}$  [26]. The tensor nuclear norm (TNN) of  $\mathcal{X}$  is subsequently defined and it equals to the sum of the nuclear norm of  $\hat{\mathcal{X}}$ ’s frontal slices and is the relaxation of the sum of matrix ranks from all  $\hat{\mathcal{X}}$ ’s slices. By minimizing the TNN, Zhang *et al.* [26] build the low-rank tensor completion model and provided theoretical performance bounds for third-order tensor recovery from limited sampling. Lu *et al.* [27] utilize the TNN<sup>1</sup> for the tensor robust principle

<sup>1</sup>In [27], the TNN is defined with a factor  $1/n_3$ .

component analysis. Similar researches, which adopt the TNN for multi-dimensional data recovery, can be found in [28–30].

Other than the Fourier transform, Kernfeld *et al.* find that the t-prod, together with the tensor decomposition scheme, can be defined via any invertible transform, for instance, the discrete cosine transform (DCT). Namely, the t-prod can be implemented by the matrices’ product after the invertible transformation along the third mode. Xu *et al.* [31] validate that, when minimizing the DCT based TNN for the tensor completion problem, the DCT is superior to the DFT in terms of the preservation of the head and the tail frontal slices, because of its mirror boundary condition. Corroborative results can be found in [32], which demonstrates that any invertible linear transform can be applied to induce the TNN for the tensor completion task. Coincidentally, Song *et al.* [33] find that the corresponding transformed tubal-rank could be approximately smaller with an appropriate unitary transform, for instance, the Haar wavelet transform, and they prove that one can recover a low transformed tubal-rank tensor exactly with overwhelming probability provided that its transformed tubal rank is sufficiently small and its corrupted entries are reasonably sparse.

The tensor data recovery within the t-SVD framework can be viewed as finding a low-rank approximation in the transformed domain. Therefore, if the transformed tensor could be approximately lower-rank, minimizing the corresponding TNN, namely the TNN defined based on the transformation, would be more effective for the recovery [33]. In [32, 33], the authors establish elegant theoretical results based on the unitary transform or the invertible linear transform. However, the requirement of the invertibility prevents their results from other non-invertible (or semi-invertible) transformations, which could bring in redundancy. We note that redundancy in the transformation is important as such transformed coefficients can contain information of missing data in the original domain, see for example the work by Cai *et al.* [34].

In this paper, we suggest to use the tight wavelet frame (framelet) as the transformation within t-SVD framework. Because of framelet basis redundancy, the representation of each tube is sparsely represented. We expect when each matrix slices of the original tensor, the corresponding sum of matrix ranks from all framelet transformed matrix slices would be small. As an example, we illustrate this motivation by using magnetic resonance image (MRI) of size  $142 \times 178 \times 121$ , multispectral image (MSI) of size  $512 \times 512 \times 31$  and video data of size  $144 \times 176 \times 100$  to demonstrate their rank reduction via framelet transformation<sup>2</sup> to the Fourier transformation. Note that for real imaging data, each transformed matrix frontal slice is not a exact low-rank matrix, but it is close to a low-rank matrix. There are many small singular values of each transformed matrix frontal slice. We show in Table I that the mean value of the matrix ranks of  $\mathcal{X}(:, :, i)$  (the  $i$ -th transformed matrix frontal slice). Here we discard the singular values of transformed matrix frontal slice when they are smaller than the truncation parameter, and the truncated rank of transformd matrix slice is obtained. It is clear that

TABLE I  
THE MEAN VALUE OF ALL THE TRUNCATED TRANSFORMED MATRIX SLICES RANKS BY USING THE FFT AND THE FRAMELET TRANSFORM FOR MRI, MSI AND VIDEO DATA SETS.

Data	Parameter $\epsilon$	FFT Multi-rank (mean value)	Framelet Multi-rank (mean value)	Reduction
MRI	0.02	101.0	77.8	23.3
	0.01	120.1	94.1	25.9
	0.005	131.9	108.9	23.0
Video	0.02	106.7	74.5	32.2
	0.01	122.7	92.2	30.5
	0.005	132.6	108.5	24.1
MSI	0.02	83.8	46.1	37.7
	0.01	132.8	77.8	55.0
	0.005	218.0	136.0	82.0

the mean value of such truncated matrix ranks by using framelet transformation is lower than that by using the Fourier transformation. When a framelet transformed tensor is close to a low-rank tensor compared with the use of the Fourier transform, it is expected that the resulting tensor completion can be performed much better in practice. A framelet based TNN (F-TNN) minimization model is subsequently formulated for the low-rank tensor completion (LRTC). The proposed minimization model is convex and global minimizers can be obtained via the alternating direction multipliers method (ADMM) [35] with a theoretical convergence guarantee. We conduct numerical experiments on various types of multi-dimensional imaging data and the results verify that our framelet based method outperforms the compared methods.

### A. Contributions

The main contributions can be summarised as follows. (i) We suggest the framelet transform within the t-SVD framework and proposed a tensor completion model, which minimizes the framelet representation of the tensor nuclear norm. (ii) To tackle the non-invertible framelet transform based model, we develop an alternating direction multipliers method (ADMM) based algorithm with guaranteed convergence, and we test our method on various types of multi-dimensional data. The outperformance of our method further corroborates the usage of framelet.

The outline of this paper is given as follows. In Section II, some preliminary background on tensors and the framelet is given. The main results, including the proposed model and algorithm, are presented in Section III. Experimental results are reported in Section IV. Finally, Section V draws some conclusions.

## II. PRELIMINARIES

This section provides the basic ingredients to induce the proposed method. We firstly give the basic tensor notations and then introduce the t-SVD framework, which has been proposed in [21, 22, 26, 27]. We restate them here at the readers’ convenience. Next, the basics of framelet are briefly presented.

<sup>2</sup>The piece-wise cubic B-spline is used to generate framelet system.

### A. Tensor Notations And Definitions

Generally, a third order tensor is denoted as  $\mathcal{X} \in \mathbb{R}^{n_1 \times n_2 \times n_3}$ , and  $x_{i,j,k}$  is its  $(i, j, k)$ -th component. We use  $\mathcal{X}^{(k)}$  or  $\mathcal{X}(:, :, k)$  to denote the  $k$ -th frontal slice of a third-order tensor  $\mathcal{X} \in \mathbb{R}^{n_1 \times n_2 \times n_3}$ . The mode-3 unfolding of a tensor  $\mathcal{X} \in \mathbb{R}^{n_1 \times n_2 \times n_3}$  is denoted as  $\mathbf{X}_{(3)} \in \mathbb{R}^{n_3 \times n_1 n_2}$ , where the tensor's  $(i, j, k)$ -th element maps to the matrix's  $(k, l)$ -th element satisfying  $l = (j-1)n_2 + i$ . The mode-3 unfolding operator and its inverse are respectively denoted as  $\text{unfold}_3$  and  $\text{fold}_3$ , and they satisfy  $\mathcal{X} = \text{fold}_3(\text{unfold}_3(\mathcal{X})) = \text{fold}_3(\mathbf{X}_{(3)})$ . We use  $\hat{\mathcal{X}}$  to denote the transformed tensor by performing discrete Fourier transform along the mode-3 fibers (tubes) of  $\mathcal{X}$ . By using the DFT matrix  $\mathbf{F}_{n_3} \in \mathbb{R}^{n_3 \times n_3}$ , we have  $\hat{\mathcal{X}} = \text{fold}_3(\mathbf{F}_{n_3} \text{unfold}_3(\mathcal{X})) \in \mathbb{R}^{n_1 \times n_2 \times n_3}$ .

**Definition 2.1 (tensor conjugate transpose [22]):** The conjugate transpose of a tensor  $\mathcal{A} \in \mathbb{C}^{n_2 \times n_1 \times n_3}$  is tensor  $\mathcal{A}^H \in \mathbb{C}^{n_1 \times n_2 \times n_3}$  obtained by conjugate transposing each of the frontal slice and then reversing the order of transposed frontal slices 2 through  $n_3$ , i.e.,  $(\mathcal{A}^H)^{(1)} = (\mathcal{A}^{(1)})^H$  and  $(\mathcal{A}^H)^{(i)} = (\mathcal{A}^{(n_3+2-i)})^H$  ( $i = 2, \dots, n_3$ ).

**Definition 2.2 (t-prod [22]):** The tensor-tensor-product (t-prod)  $\mathcal{C} = \mathcal{A} * \mathcal{B}$  of  $\mathcal{A} \in \mathbb{R}^{n_1 \times n_2 \times n_3}$  and  $\mathcal{B} \in \mathbb{R}^{n_2 \times n_4 \times n_3}$  is a tensor of size  $n_1 \times n_4 \times n_3$ , where the  $(i, j)$ -th tube  $\mathbf{c}_{ij}$ : is given by

$$\mathbf{c}_{ij} = \mathcal{C}(i, j, :) = \sum_{k=1}^{n_2} \mathcal{A}(i, k, :) * \mathcal{B}(k, j, :) \quad (1)$$

where  $*$  denotes the circular convolution between two tubes of same size.

**Definition 2.3 (identity tensor [22]):** The identity tensor  $\mathcal{I} \in \mathbb{R}^{n_1 \times n_1 \times n_3}$  is the tensor whose first frontal slice is the  $n_1 \times n_1$  identity matrix, and whose other frontal slices are all zeros.

**Definition 2.4 (orthogonal tensor [22]):** A tensor  $\mathcal{Q} \in \mathbb{C}^{n_1 \times n_1 \times n_3}$  is orthogonal if it satisfies

$$\mathcal{Q}^H * \mathcal{Q} = \mathcal{Q} * \mathcal{Q}^H = \mathcal{I}. \quad (2)$$

**Definition 2.5 (f-diagonal tensor [22]):** A tensor  $\mathcal{A}$  is called f-diagonal if each frontal slice  $\mathcal{A}^{(i)}$  is a diagonal matrix.

**Theorem 2.1 (t-SVD [21, 22]):** For  $\mathcal{A} \in \mathbb{R}^{n_1 \times n_2 \times n_3}$ , the t-SVD of  $\mathcal{A}$  is given by

$$\mathcal{A} = \mathcal{U} * \mathcal{S} * \mathcal{V}^H \quad (3)$$

where  $\mathcal{U} \in \mathbb{R}^{n_1 \times n_1 \times n_3}$  and  $\mathcal{V} \in \mathbb{R}^{n_2 \times n_2 \times n_3}$  are orthogonal tensors, and  $\mathcal{S} \in \mathbb{R}^{n_1 \times n_2 \times n_3}$  is an f-diagonal tensor. The t-SVD is illustrated in Figure 1.

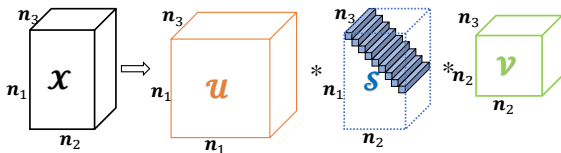


Fig. 1. The t-SVD of an  $n_1 \times n_2 \times n_3$  tensor.

**Definition 2.6 (tensor tubal-rank and multi-rank [26]):** The tubal-rank of a tensor  $\mathcal{A} \in \mathbb{R}^{n_1 \times n_2 \times n_3}$ , denoted as  $\text{rank}_t(\mathcal{A})$ ,

is defined to be the number of non-zero singular tubes of  $\mathcal{S}$ , where  $\mathcal{S}$  comes from the t-SVD of  $\mathcal{A}$ :  $\mathcal{A} = \mathcal{U} * \mathcal{S} * \mathcal{V}^T$ . That is

$$\text{rank}_t(\mathcal{A}) = \#\{i : \mathcal{S}(i, :, :) \neq 0\}. \quad (4)$$

The tensor multi-rank of  $\mathcal{A} \in \mathbb{R}^{n_1 \times n_2 \times n_3}$  is a vector, denoted as  $\text{rank}_r(\mathcal{A}) \in \mathbb{R}^{n_3}$ , with the  $i$ -th element equals to the rank of  $i$ -th frontal slice of  $\hat{\mathcal{A}}$ .

**Definition 2.7 (block diagonal form [26]):** Let  $\bar{\mathcal{A}}$  denote the block-diagonal matrix of the tensor  $\hat{\mathcal{A}}$  in the Fourier domain, i.e.,

$$\bar{\mathcal{A}} \triangleq \text{blockdiag}(\hat{\mathcal{A}}) \triangleq \begin{bmatrix} \hat{\mathcal{A}}^{(1)} & & & \\ & \hat{\mathcal{A}}^{(2)} & & \\ & & \ddots & \\ & & & \hat{\mathcal{A}}^{(n_3)} \end{bmatrix} \in \mathbb{C}^{n_1 n_3 \times n_2 n_3}, \quad (5)$$

where  $\hat{\mathcal{A}}^{(k)} = \hat{\mathcal{A}}(:, :, k)$  is the  $k$ -th slice of  $\hat{\mathcal{A}}$  for  $k = 1, 2, \dots, n_3$ .

It is not difficult to find that  $\bar{\mathcal{A}}^H = \bar{\mathcal{A}}^H$ , i.e., the block diagonal form of a tensor's conjugate transpose equals to the matrix conjugate transpose of the tensor's block diagonal form. Further more, for any tensor  $\mathcal{A} \in \mathbb{R}^{n_1 \times n_2 \times n_3}$  and  $\mathcal{B} \in \mathbb{R}^{n_2 \times n_4 \times n_3}$ , we have

$$\mathcal{A} * \mathcal{B} = \mathcal{C} \Leftrightarrow \bar{\mathcal{A}} \cdot \bar{\mathcal{B}} = \bar{\mathcal{C}},$$

where  $\cdot$  is the matrix product.

**Definition 2.8 (tensor-nuclear-norm (TNN) [26]):** The tensor nuclear norm of a tensor  $\mathcal{A} \in \mathbb{R}^{n_1 \times n_2 \times n_3}$ , denoted as  $\|\mathcal{A}\|_{\text{TNN}}$ , is defined as

$$\|\mathcal{A}\|_{\text{TNN}} \triangleq \|\bar{\mathcal{A}}\|_*. \quad (6)$$

The TNN can be computed via the summation of the matrix nuclear norm of Fourier transformed tensor's slices. That is  $\|\mathcal{A}\|_{\text{TNN}} = \sum_{i=1}^{n_3} \|\hat{\mathcal{A}}^{(i)}\|_*$ .

We summary the frequent used notations in Table II-A.

TABLE II  
TENSOR NOTATIONS

Notation	Explanation
$\mathcal{X}, \mathbf{X}, \mathbf{x}, x$	Tensor, matrix, vector, scalar.
$*$	The tensor-tensor product or the circular convolution between vectors.
$\mathcal{X}(:, :, k)$ (or $\mathcal{X}^{(k)}$ )	The $k$ -th frontal slice of a third-order tensor $\mathcal{X} \in \mathbb{R}^{n_1 \times n_2 \times n_3}$ .
$\text{fold}_3$ ( $\text{unfold}_3$ )	The fold (or unfold) operation along the third mode.
$\mathbf{X}_{(3)}$	The mode-3 unfolding of a tensor $\mathcal{X}$ .
$\hat{\mathcal{X}}$	The Fourier transformed (along the third mode) tensor.
$\text{rank}_r(\mathcal{A})$	The multi-rank of a tensor $\mathcal{X}$ and its $i$ -th element equals to $\text{rank}(\hat{\mathcal{X}}^{(i)})$ .
$\ \mathcal{X}\ _{\text{TNN}}$	The tensor nuclear norm of a tensor $\mathcal{X}$ and it equals to the sum of the nuclear norms of $\hat{\mathcal{X}}$ 's slices.

### B. Framelet

A tight frame is defined as a countable set  $X \subset L_2(\mathbb{R})$  with the property that  $\forall f \in L_2(\mathbb{R}), f = \sum_{g \in X} \langle f, g \rangle g$ . This is equivalent to that  $\forall f \in L_2(\mathbb{R})$ , we have

$$\|f\|_{L_2(\mathbb{R})}^2 = \sum_{g \in X} |\langle f, g \rangle|^2,$$

where  $\langle \cdot, \cdot \rangle$  is the inner product in  $L^2(\mathbb{R})$ , and  $\|\cdot\|_{L^2(\mathbb{R})} = \langle \cdot, \cdot \rangle^{\frac{1}{2}}$ .

For given  $\Psi := \{\psi_1, \psi_2, \dots, \psi_r\} \subset L^2(\mathbb{R})$ , the affine (or wavelet) system is defined by the collection of the dilations and the shifts of  $\Psi$  as  $X(\Psi) := \{\psi_{l,j,k} : 1 \leq l \leq r; j, k \in \mathbb{Z}\}$ , where  $\psi_{l,j,k} := 2^{j/2} \psi_l(2^j \cdot -k)$ . When  $X(\Psi)$  forms a tight frame of  $L^2(\mathbb{R})$ , it is called a tight wavelet frame, and  $\psi_l, l = 1, 2, \dots, r$  are called the (tight) framelets. In the numerical scheme of image processing, the framelet transform (decomposition operator) of a vector  $\mathbf{v} \in \mathbb{R}^n$  can be represented by a matrix  $\mathbf{W} \in \mathbb{R}^{wn \times n}$  is the framelet transform matrix constructed with  $n$  filters and  $l$  levels and  $w = (n-1)l + 1$ . The processes of generating such matrices have been detailed in many literatures such as [34, 36]. We omit them here for readability. Then the framelet transform of a discrete signal  $\mathbf{v} \in \mathbb{R}^n$ , can be written as  $\mathbf{u} = \mathbf{W}\mathbf{v} \in \mathbb{R}^{wn}$ . Besides, the unitary extension principle (UEP) [37] asserts that  $\mathbf{W}^T \mathbf{W}\mathbf{v} = \mathbf{v}$ , where  $\mathbf{W}^T$  indicates the inverse framelet transform. However,  $\mathbf{W}\mathbf{W}^T \mathbf{u} \neq \mathbf{u}$ .

### III. THE PROPOSED MODEL AND ALGORITHM

In this section, we replace the Fourier transform by the framelet transform. The starting point of our idea is that the framelet transform would bring in redundancy and the transformed data is of lower multi-rank. Then we build the low-rank tensor completion model based on the framelet representation of the tensor nuclear norm and propose the ADMM based algorithm to optimize this model.

#### A. From DFT to The Framelet Transformation

For a three way tensor  $\mathcal{X} \in \mathbb{R}^{n_1 \times n_2 \times n_3}$ , owing to the circular convolution in Def. 2.2, its t-SVD can be efficiently computed. The DFT plays an important role in tensor-tensor product, and the DFT on  $\mathbf{v} \in \mathbb{R}^n$ , denoted as  $\bar{\mathbf{v}}$ , is given by  $\bar{\mathbf{v}} = \mathbf{F}_n \mathbf{v} \in \mathbb{C}^n$ , where  $\mathbf{F}_n$  is the DFT matrix. Note that  $\mathbf{F}_n / \sqrt{n}$  is an orthogonal matrix, i.e.,  $\mathbf{F}_n^* \mathbf{F}_n = \mathbf{F}_n \mathbf{F}_n^* = n \mathbf{I}_n$ . Therefore  $\mathbf{F}_n^{-1} = \mathbf{F}_n^* / n$ . Computing  $\bar{\mathbf{v}}$  by using the DFT matrix costs  $O(n^2)$ . By using the DFT matrix, for a tensor  $\mathcal{X} \in \mathbb{R}^{n_1 \times n_2 \times n_3}$ , we have

$$\hat{\mathcal{X}} = \text{fold}_3(\mathbf{F}_{n_3} \mathbf{X}_{(3)}) \in \mathbb{R}^{n_1 \times n_2 \times wn_3},$$

where  $\mathbf{X}_{(3)}$  is the mode-3 unfolding of  $\mathcal{X}$

Next, we will adopt the framelet transform as a substitute for the Fourier transform, and give the definition of the framelet representation of the tensor nuclear norm. For simplicity, we denote the tensor after framelet transform along the third mode as

$$\mathcal{X}_{\mathbf{W}} = \text{fold}_3(\mathbf{W}\mathbf{X}_{(3)}) \in \mathbb{R}^{n_1 \times n_2 \times wn_3},$$

where  $\mathbf{W} \in \mathbb{R}^{wn_3 \times n_3}$  is the framelet transform matrix constructed with  $n$  filters and  $l$  levels and  $w = (n-1)l + 1$ .

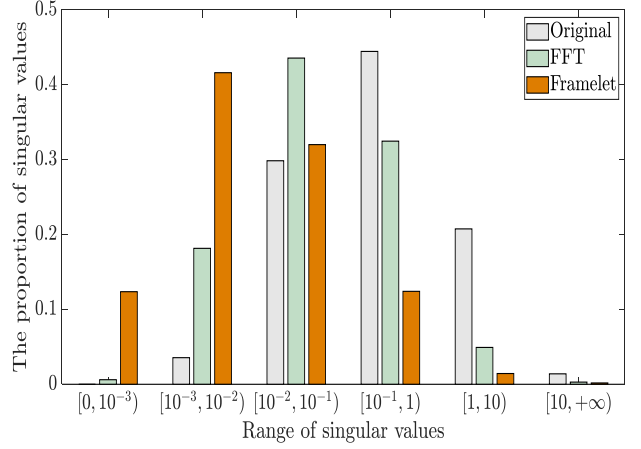


Fig. 2. The distribution of singular values. Here, the singular values are obtained by conducting SVD on each frontal slice of the original tensor data or the transformed tensors.

Considering the UEP property of the framelet transform, we have  $\mathcal{X} = \text{fold}_3(\mathbf{W}^T [\mathbf{X}_{\mathbf{W}}]_{(3)})$ , where  $[\mathbf{X}_{\mathbf{W}}]_{(3)} = \text{unfold}_3(\mathcal{X}_{\mathbf{W}})$ .

Recalling Def. 2.6, the tensor multi-rank is defined as a vector of the ranks of the frontal slices in the Fourier transform domain. Therefore, the framelet based multi-rank is defined in the same manner as followings.

**Definition 3.1 (Framelet based multi-rank):** The framelet based multi-rank of a tensor  $\mathcal{X} \in \mathbb{R}^{n_1 \times n_2 \times n_3}$  is defined as a vector  $\mathbf{r}_w \in \mathbb{R}^{wn_3}$  with the  $i$ -th elements  $\mathbf{r}_w(i) = \text{rank}(\mathcal{X}_{\mathbf{W}}(:, :, i))$  for  $i = 1, 2, \dots, wn_3$ .

Here we have replaced the Fourier transform by the framelet and defined the framelet based multi-rank. As mentioned before, the framelet transformed tensor can be of lower (framelet based) multi-rank. To understand this in depth, we give some empirically numerical analyses on the singular values of the frontal slices of the transformed tensors. Here, taking the video data news<sup>3</sup> as an example, the original video data is denoted as  $\mathcal{X} \in \mathbb{R}^{144 \times 176 \times 100}$  and its Fourier and framelet transformed tensors are denoted as  $\hat{\mathcal{X}}$  and  $\mathcal{X}_{\mathbf{W}}$ , respectively. In Figure 2, we exhibit the distributions of the singular values of the frontal slices of  $\mathcal{X}$ , the Fourier transformed tensors  $\hat{\mathcal{X}}$  and the framelet transformed tensors  $\mathcal{X}_{\mathbf{W}}$ . In Figure 2, we show the proportion of the number of singular values of transformed matrix frontal slices in each magnitude interval. It can be found in the figure that a large proportion of the singular values of the framelet transformed data appears in the interval of  $[0, 10^{-2}]$  compared with the original video data and the Fourier transformed tensor  $\hat{\mathcal{X}}$ . This phenomenon brings in an advantage that the data can be better approximated with lower rank via the framelet representation. In Section 4, we will illustrate tensor completion can be obtained by using the framelet representation.

<sup>3</sup>Data available at <http://trace.eas.asu.edu/yuv/>.

<sup>4</sup>The piece-wise cubic B-spline is used to generate framelet system.

### B. Tensor Completion via Minimizing The Framelet Based TNN

Using the DFT matrix  $\mathbf{F}_{n_3}$ , the tensor nuclear norm in (6) of a tensor  $\mathcal{X} \in \mathbb{R}^{n_1 \times n_2 \times n_3}$  can be expressed as

$$\begin{aligned} \|\mathcal{X}\|_{\text{TNN}} &= \|\overline{\mathcal{X}}\|_* = \sum_{i=1}^{n_3} \|\widehat{\mathcal{X}}^{(i)}\|_* \\ &= \sum_{i=1}^{n_3} \|\text{fold}_3(\mathbf{F}_{n_3} \mathbf{X}_{(3)})(:, :, k)\|_*, \end{aligned} \quad (7)$$

where  $\mathbf{X}_{(3)}$  is the mode-3 unfolding of  $\mathcal{X}$ .

**Definition 3.2 (Framelet based TNN (F-TNN)):** Similarly, the framelet representation of the tensor nuclear norm can be formulated as

$$\begin{aligned} \|\mathcal{X}\|_{\text{F-TNN}} &= \|\text{blockdiag}(\mathcal{X}_{\mathbf{W}})\|_* = \sum_{k=1}^{wn_3} \|\mathcal{X}_{\mathbf{W}}(:, :, k)\|_* \\ &= \sum_{k=1}^{wn_3} \|\text{fold}_3(\mathbf{W} \mathbf{X}_{(3)})(:, :, k)\|_*, \end{aligned} \quad (8)$$

where  $\mathbf{W} \in \mathbb{R}^{wn_3 \times n_3}$  is the framelet transform matrix.

It is not difficult to obtain that the F-TNN is a convex envelope of the  $\ell_1$  norm of the framelet based multi-rank. Afterwards, our tensor completion model, which is convex, is formulated as

$$\begin{aligned} \min_{\mathcal{X}} \quad & \|\mathcal{X}\|_{\text{F-TNN}} \\ \text{s.t.} \quad & \mathcal{X}_{\Omega} = \mathcal{O}_{\Omega}, \end{aligned} \quad (9)$$

where  $\mathcal{O} \in \mathbb{R}^{n_1 \times n_2 \times n_3}$  is the incomplete observed data, and  $\Omega$  set of indexes of the observed entries.  $\mathcal{X}_{\Omega} = \mathcal{O}_{\Omega}$  constrains that the entries of  $\mathcal{X}$  should agree with  $\mathcal{O}$  in  $\Omega$ .

### C. Optimization

Let

$$\mathcal{I}_{\Phi}(\mathcal{X}) = \begin{cases} 0, & \mathcal{X} \in \Phi, \\ \infty, & \text{otherwise,} \end{cases} \quad (10)$$

where  $\Phi := \{\mathcal{X} \in \mathbb{R}^{n_1 \times n_2 \times n_3}, \mathcal{X}_{\Omega} = \mathcal{O}_{\Omega}\}$ .

Thus, the problem (9) can be rewritten as

$$\min_{\mathcal{X}} \quad \mathcal{I}_{\Phi}(\mathcal{X}) + \sum_{k=1}^{wn_3} \|\mathcal{X}_{\mathbf{W}}(:, :, k)\|_* \quad (11)$$

Then, the minimization problem (11) can be efficiently solved via ADMM [35].

After introducing the auxiliary variable  $\mathcal{V}$ , the problem (11) can be rewritten as the following unconstraint problem

$$\begin{aligned} \min_{\mathcal{X}} \quad & \mathcal{I}_{\Phi}(\mathcal{X}) + \sum_{k=1}^{wn_3} \|\mathcal{V}(:, :, k)\|_* \\ \text{s.t.} \quad & \mathcal{V} = \mathcal{X}_{\mathbf{W}}. \end{aligned} \quad (12)$$

The augmented Lagrangian function of (12) is given by

$$\begin{aligned} L_{\beta}(\mathcal{X}, \mathcal{V}, \Lambda) &= \mathcal{I}_{\Phi}(\mathcal{X}) + \sum_{k=1}^{wn_3} \|\mathcal{V}(:, :, k)\|_* \\ &+ \frac{\beta}{2} \|\mathcal{X}_{\mathbf{W}} - \mathcal{V} + \frac{\Lambda}{\beta}\|_F^2 \end{aligned} \quad (13)$$

where  $\Lambda \in \mathbb{R}^{n_1 \times n_2 \times wn_3}$  is the Lagrangian multiplier,  $\beta$  is the penalty parameter for the violation of the linear constraints. In the scheme of the ADMM, we update each variable alternately.

**$\mathcal{V}$  sub-problem:** The  $\mathcal{V}$  at  $t$ -th iteration is

$$\mathcal{V}^{t+1} = \arg \min_{\mathcal{V}} \sum_{k=1}^{wn_3} \|\mathcal{V}(:, :, k)\|_* + \frac{\beta}{2} \|\mathcal{X}_{\mathbf{W}}^t - \mathcal{V} + \frac{\Lambda^t}{\beta}\|_F^2 \quad (14)$$

Then, (14) can be decomposed into  $wn_3$  subproblems and it is easy to obtain the closed form solution of these subproblems with the singular value thresholding (SVT) operator [38]. Hence, we update  $\mathcal{V}$  as

$$\mathcal{V}^{t+1}(:, :, k) = \text{SVT}_{\frac{1}{\beta}} \left( \mathcal{X}_{\mathbf{W}}^t(:, :, k) + \frac{\Lambda^t(:, :, k)}{\beta} \right), \quad (15)$$

where  $k = 1, 2, \dots, wn_3$ .

**$\mathcal{X}$  sub-problem:** For convenience, the subproblem of optimizing  $L_{\beta}$  with respect to  $\mathcal{X}$  at  $t$ -th iteration is written in the matrix format as (recalling that  $\mathcal{X}_{\mathbf{W}} = \text{fold}_3(\mathbf{W} \mathbf{X}_{(3)})$ )

$$\mathbf{X}^{t+1} = \arg \min_{\mathbf{X}} \mathcal{I}_{\Phi}(\mathcal{X}) + \frac{\beta}{2} \|\mathbf{W} \mathbf{X} - \mathbf{V}_{(3)}^{t+1} + \frac{\Lambda_{(3)}^t}{\beta}\|_F^2, \quad (16)$$

where  $\mathbf{V}_{(3)}^{t+1} = \text{unfold}_3(\mathcal{V}^{t+1})$  and  $\Lambda_{(3)}^t = \text{unfold}_3(\Lambda^t)$ . To optimize (16), we first solve the following equation

$$\mathbf{W}^{\top} \mathbf{W} \mathbf{X}_{(3)} = \mathbf{W}^{\top} \left( \mathbf{V}_{(3)}^{t+1} - \frac{\Lambda_{(3)}^t}{\beta} \right). \quad (17)$$

Thus, considering that  $\mathbf{W}^{\top} \mathbf{W} \mathbf{X}_{(3)} = \mathbf{X}_{(3)}$  (the UEP property of the framelet transformation), we have

$$\mathcal{X}^{t+1} = \mathcal{P}_{\Omega^c} \left( \text{fold}_3 \left( \frac{1}{2} \mathbf{W}^{\top} \left( \mathbf{V}_{(3)}^{t+1} - \frac{\Lambda_{(3)}^t}{\beta} \right) \right) \right) + \mathcal{P}_{\Omega}(\mathcal{O}), \quad (18)$$

where  $\mathcal{P}_{\Omega}(\cdot)$  is the projection function that keeps the entries of  $\cdot$  in  $\Omega$  while making others be zeros, and  $\Omega^c$  denotes the complementary set of  $\Omega$ . Meanwhile, we have  $\mathcal{X}_{\mathbf{W}}^{t+1} = \text{fold}_3(\mathbf{W} \mathbf{X}_{(3)}^{t+1})$ .

**Updating the multiplier:** The multiplier  $\Lambda$  can be updated by

$$\Lambda^{t+1} = \Lambda^t + \beta (\mathcal{X}_{\mathbf{W}}^{t+1} - \mathcal{V}^{t+1}). \quad (19)$$

Finally, our algorithm is summarized in Algorithm 1. The objective function of the proposed model in (9) is convex. Our algorithm fits the standard ADMM framework and its convergence is theoretically guaranteed [35].

## IV. NUMERICAL EXPERIMENTS

In this section, to illustrate the performance of the proposed method, we will exhibit the experimental results on three typical kinds of third-order data, i.e., the MRI data, the MSI data, and the video data. Three numerical metrics, consisting of the peak signal-to-noise ratio (PSNR), the structural similarity index (SSIM) [39], and the feature similarity index (FSIM) [40] are selected to quantitatively measure the reconstructed results. On account of that the data are third order tensors, we report the mean PSNR (MPSNR), the mean SSIM (MSSIM), and the mean FISM (MFSIM) of all the frontal slices.

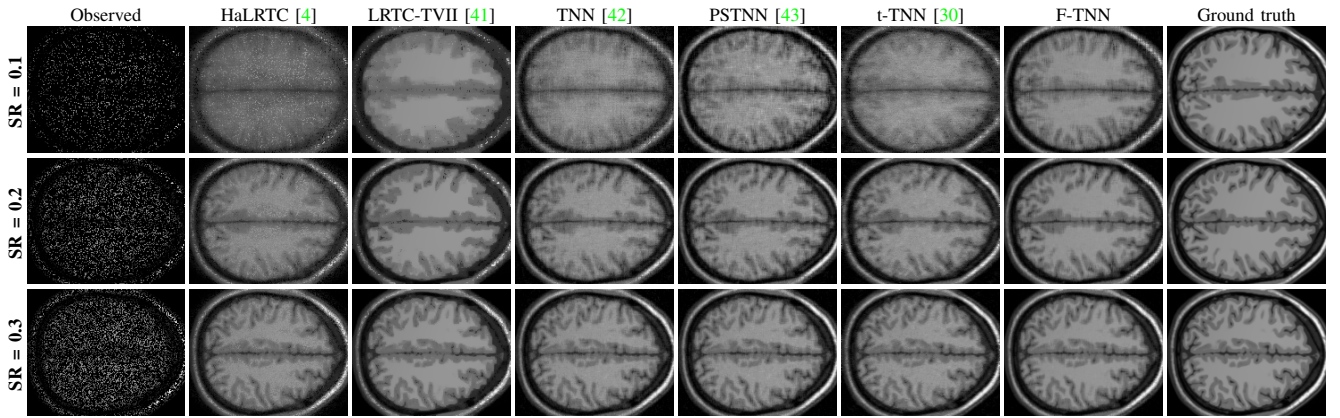


Fig. 3. The visual illustration of the results on the *MRI* data by different methods with different sampling rates (SR). From left to right are the frontal slices of observed incomplete data, results by different methods and the ground truth, respectively. From top to bottom are respectively corresponding to the 106-th slice, the 110-th slice and the 115-th slice.

---

#### Algorithm 1 Tensor completion via minimizing F-TNN

---

**Input:** The observed incomplete tensor  $\mathcal{O} \in \mathbb{R}^{n_1 \times n_2 \times n_3}$ ; the support  $\Omega$ .

**Initialization:**  $\mathcal{X}^{(0)} = \text{rand}(n_1 \times n_2 \times n_3)$  and  $\mathcal{X}_\Omega^{(0)} = \mathcal{O}_\Omega$ ;  $\beta = 1.0$ ; the framelet transform matrix  $\mathbf{W}$ .

- 1: **while** not converged **do**
- 2:   Update  $\mathcal{V}$  via Eq. (15);
- 3:   Update  $\mathcal{X}$  via Eq. (18);
- 4:   Update  $\Lambda$  Eq. (19).
- 5: **end while**

**Output:** The reconstructed tensor  $\mathcal{X}$ .

---

**Experimental Settings:** We generated the framelet system via the piece-wise cubic B-spline. If not specified, the parameters are set as followings. The framelet decomposition level  $l$  is set as 4 ( $l = 2$  for the MSI data), and the Lagrangian penalty parameter  $\beta = 1$ . The maximum iteration of our algorithm and the convergence tolerance are respectively chosen as 100 and  $1e-2$ . All the methods are implemented on the platform of Windows 10 and Matlab (R2017a) with an Intel(R) Core(TM) i5-4590 CPU at 3.30GHz and 16 GB RAM.

**Compared Methods:** We compare our method with five tensor completion methods, including a baseline method HaLRTC [4], a TNN based method [42], a non-convex method minimize the partial sum of the TNN (PSTNN) [43], the twist TNN (t-TNN) method [30], and a total variation based method LRTC-TVII [41].

#### A. MRI Data

In this subsection, we evaluate the performance of the proposed method and the compared methods on the MRI data<sup>5</sup>, which is of size  $142 \times 178 \times 121$ . As shown in Fig. 3, this is an MRI of the brain, which consists of abundance textures of the gray matter and the white matter. The sampling rates (SR) are set as 10%, 20%, and 30%.

Table III shows the quantitative assessments of the results recovered by different methods. Form Table III, it can be

found that the proposed method reaches the highest indices for different sampling rates. The non-convex method PSTNN obtains the second best PSNR and the performance of the total variation based method LRTC-TVII is promising considering the SSIM and the FSIM. The margins between the results by our method and the second best results are more than 1.5dB considering the PSNR, and 0.02 with respect to the SSIM and FSIM.

TABLE III  
QUANTITATIVE COMPARISONS OF THE *MRI* DATA RECOVERY RESULTS OF FALRTC [4], LRTC-TVII [41], TNN [42], PSTNN [43], t-TNN [30] AND THE PROPOSED METHOD. THE BEST VALUES AND THE SECOND BEST VALUES ARE RESPECTIVELY HIGHLIGHTED BY BOLDER FONTS AND UNDERLINES.

SR	Index	Observed	HaLRTC	LRTC-TVII	TNN	PSTNN	t-TNN	F-TNN
10%	PSNR	9.049	18.012	21.965	21.855	<u>24.578</u>	21.774	<b>26.104</b>
	SSIM	0.047	0.388	<u>0.665</u>	0.524	<u>0.628</u>	0.527	<b>0.759</b>
	FSIM	0.475	0.686	0.765	0.760	<u>0.802</u>	0.756	<b>0.862</b>
20%	PSNR	9.561	23.404	26.531	27.301	<u>28.566</u>	27.431	<b>30.207</b>
	SSIM	0.073	0.657	<u>0.838</u>	0.776	0.806	0.789	<b>0.886</b>
	FSIM	0.523	0.823	<u>0.885</u>	0.871	0.885	0.874	<b>0.925</b>
30%	PSNR	10.141	26.896	29.633	30.897	<u>31.382</u>	31.091	<b>33.142</b>
	SSIM	0.103	0.794	<u>0.910</u>	0.880	0.885	0.893	<b>0.936</b>
	FSIM	0.550	0.892	<u>0.935</u>	0.925	0.928	0.930	<b>0.956</b>

We illustrate one frontal slice of the results by different methods with different random sampling rates in Fig. 3. As shown in the top row of Fig. 3, when the sampling rate is 10%, the proposed method accurately reconstructs the MRI data, with a clear margin of the gray matter and the white matter. From the third column, we can conclude that the results by LRTC-TVII are over-smoothed. When the sampling rate is 30%, all the method get good performances, and the white matter regions recovered by the proposed method and LRTC-TVII are the visually best.

#### B. MSI Data

In this subsection, we evaluate the performance of our method and the compared methods on 32 MSIs<sup>6</sup> from the

<sup>5</sup>[http://brainweb.bic.mni.mcgill.ca/brainweb/selection\\_normal.html](http://brainweb.bic.mni.mcgill.ca/brainweb/selection_normal.html).

<sup>6</sup><http://www.cs.columbia.edu/CAVE/databases/multispectral/>.

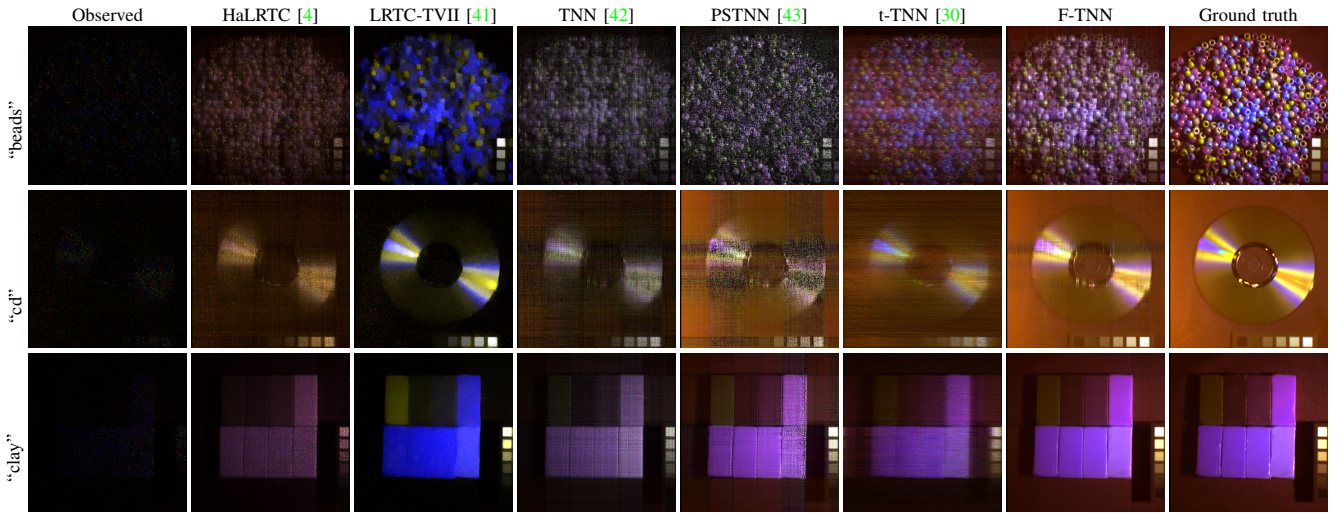


Fig. 4. The pseudo-color images (R-1 G-2 B-31) of the results on the *MSI data* “beads” (top row), “cd” (mid row), and “clay” (bottom row) by different methods, respectively, with the sampling rate = 0.05. From left to right are the observed incomplete data, results by different methods and the ground truth, respectively. For better visualization, the intensity of the pixels are adjusted.

CAVE databases [44]. The size of the MSIs is  $512 \times 512 \times 31$ , where the spatial resolution is  $512 \times 512$  and the spectral resolution is 31. The sampling rates (SR) are set as 5%, 10%, and 20%<sup>7</sup>.

The average quantitative assessments of all the results by different methods are listed in Table IV. We can find that the proposed method achieves the best performance while LRTC-TVII, PSTNN, and t-TNN obtain the second best metrics on occasions. When the sampling rate is 20%, owing to the strong correlation along the spectral direction, the performance of t-TNN is close to that of our method.

TABLE IV

THE AVERAGE MPSNR, MSSIM AND MFSIM OF THE RECOVERY RESULTS ON 32 *MSIs* BY FALRTC [4], LRTC-TVII [41], TNN [42], PSTNN [43], t-TNN [30] AND THE PROPOSED METHOD WITH DIFFERENT SAMPLING RATES. THE **BEST** VALUES AND THE SECOND BEST VALUES ARE RESPECTIVELY HIGHLIGHTED BY BOLDER FONTS AND UNDERLINES.

SR	Index	Observed	HaLRTC	LRTC-TVII	TNN	PSTNN	t-TNN	F-TNN
5%	PSNR	14.718	17.831	<u>28.283</u>	21.863	23.073	22.247	<b>33.536</b>
	SSIM	0.232	0.655	<u>0.849</u>	0.694	0.732	0.719	<b>0.917</b>
	FSIM	0.697	0.799	<u>0.893</u>	0.836	0.856	0.839	<b>0.955</b>
10%	PSNR	14.954	22.369	31.529	31.165	<u>33.945</u>	31.798	<b>38.415</b>
	SSIM	0.275	0.771	0.911	0.884	<u>0.925</u>	0.912	<b>0.969</b>
	FSIM	0.718	0.876	0.941	0.939	<u>0.961</u>	0.948	<b>0.984</b>
20%	PSNR	15.464	33.004	35.728	40.077	41.944	<u>42.228</u>	<b>43.557</b>
	SSIM	0.358	0.926	0.956	0.973	0.980	<u>0.988</u>	<b>0.989</b>
	FSIM	0.740	0.963	0.974	0.987	0.991	<u>0.993</u>	<b>0.995</b>

The third dimension of the MSI represents the spectral information and facilitates a fine delivery of more faithful knowledge under real scenes [45]. Therefore, in Fig. 4, we illustrate the pseudo-color images (Red-1 Green-2 Blue-31) of the results on the MSI data “beads”, “cd”, and “clay”, with the sampling rate = 0.05. From the similarity of the color between the results and the ground truth, we can recognize the

<sup>7</sup>For the MSI data, when the sampling rate is higher than 20%, all the methods achieve very high performances and the results are very close to the ground truths. Therefore, we select the lower sampling rates to exhibit.

spectral distortion. Although LRTC-TVII obtains the second best performance when the sampling rate is 0.05 in Table IV, we can find that the results by LRTC-TVII are spectrally distorted from Fig. 4. The superior of the proposed F-TNN is visually obvious, considering the reconstruction of the image and preservation of spectral information.

### C. Video Data

In this subsection, 9 videos<sup>8</sup> with the size  $144 \times 176 \times 100$  are selected as the ground truth third-order data. The content of these videos are different, consisting of humans, roads, rivers, cars, boats, bridges, walls and so on. The scenarios in some videos are more static while in others are more dynamic.

TABLE V

THE AVERAGE MPSNR, MSSIM AND MFSIM OF THE RECOVERY RESULTS ON 9 *videos* BY FALRTC [4], LRTC-TVII [41], TNN [42], PSTNN [43], t-TNN [30] AND THE PROPOSED METHOD WITH DIFFERENT SAMPLING RATES. THE **BEST** VALUES AND THE SECOND BEST VALUES ARE RESPECTIVELY HIGHLIGHTED BY BOLDER FONTS AND UNDERLINES.

SR	Index	Observed	HaLRTC	LRTC-TVII	TNN	PSTNN	t-TNN	F-TNN
10%	PSNR	6.176	19.936	24.476	26.411	<u>29.118</u>	25.332	<b>30.654</b>
	SSIM	0.018	0.567	0.774	0.758	<u>0.809</u>	0.733	<b>0.880</b>
	FSIM	0.423	0.773	0.825	0.875	<u>0.904</u>	0.854	<b>0.931</b>
20%	PSNR	6.687	30.150	27.656	31.329	<u>32.012</u>	31.780	<b>33.568</b>
	SSIM	0.031	0.871	0.869	0.871	<u>0.876</u>	<u>0.889</u>	<b>0.927</b>
	FSIM	0.413	0.927	0.906	0.934	0.937	<u>0.941</u>	<b>0.957</b>
30%	PSNR	7.266	32.977	30.205	34.050	34.056	<u>35.166</u>	<b>35.820</b>
	SSIM	0.046	0.917	0.917	0.915	0.912	<u>0.936</u>	<b>0.951</b>
	FSIM	0.408	0.952	0.944	0.956	0.956	<u>0.966</u>	<b>0.971</b>

Table V lists the average MPSNR, MSSIM, and MFSIM on these 9 videos with different sampling rates. For different sampling rates, although the running time of the proposed method is the second longest, our F-TNN obtains the results with the best quantitative metrics. When the sampling rate is 10%, the non-convex method PSTNN acquires the second best performance. The t-TNN ranks second with the sampling rate

<sup>8</sup><http://trace.eas.asu.edu/yuv/>.

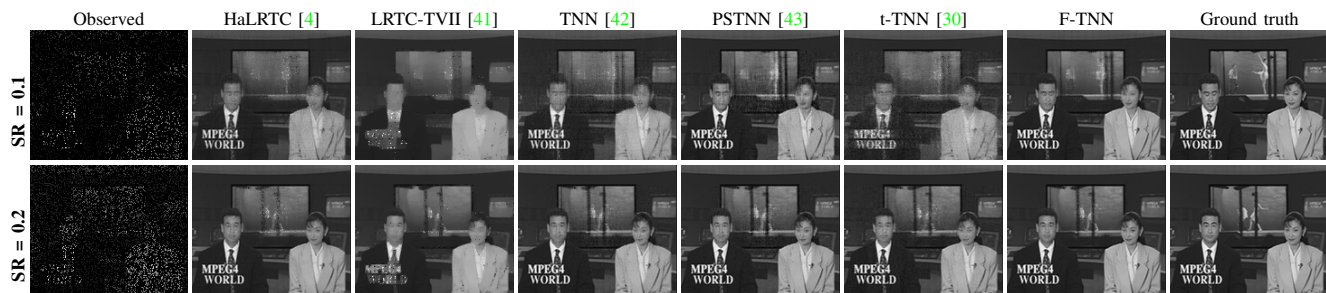


Fig. 5. The results on the *video data* “news” different methods with different sampling rates. From left to right are the observed incomplete data, results by different methods and the ground truth, respectively. From top to bottom are respectively the 15-th frame and the 67-th frame.

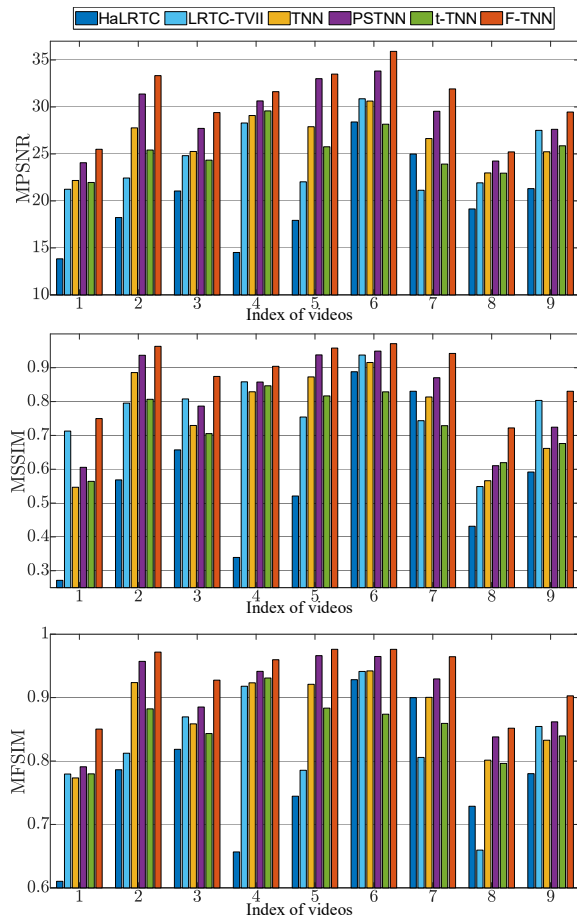


Fig. 6. The MPNSR, MSSIM, and MFSIM of the results by different methods on all the video data with the sampling rate 10%.

of 20%. While the PSNR of the results by LRTC-TVII is not high in the cases sampling rate 20% and 30%, the SSIM and FSIM indices are not low. This situation may be caused by the fact that the total variation in LRTC-TVII preserves the edges and structures well but unavoidably erases some details.

Fig. 5 exhibits the frames of the results on the videos, “news” with sampling rates 10% and 20%. As for the video “news”, there are two dynamic parts, which are the two newscasters in the front position and a playing screen in the back. The proposed method obtains the best recovering performances on both the two newscasters and the dynamic screen.

To further illustrate the performance of all the methods on different videos, in Fig. 6 we exhibit the PSNR, SSIM, and FSIM on all the videos by all the methods when the sampling rate is 10%. It can be observed that the proposed method obtains the highest PSNR, SSIM, and FISM on all the videos. This validates the robustness of our F-TNN.

#### D. Parameter Analysis

In this subsection, we evaluate the performance of the proposed method with different Framelet transformation settings and the effect from the parameter in our algorithm. Firstly, including the piece-wise cubic B-spline (denoted as “cubic”), we also adopted the Haar wavelet (denoted as “Haar”) and the piece-wise linear B-spline (denoted as “linear”) to generate the framelet transformation. Meanwhile, we also set the decomposition levels from 1 to 5. The quantitative metrics of the results obtained by the proposed method with different framelet settings are reported in Table VI. From Table VI, we can find that the piece-wise cubic B-spline is the best choice. As the decomposition level arise, the performance of the proposed method becomes better until level 5.

TABLE VI  
THE MPNSR, MSSIM AND MFSIM OF THE RECOVERY RESULTS ON THE MRI DATA BY THE PROPOSED METHOD WITH DIFFERENT FRAMELET SETTINGS. THE BEST VALUES ARE HIGHLIGHTED BY BOLDER FONTS.

Filters	Index	Level = 1	Level = 2	Level = 3	Level = 4	level = 5
Haar	PSNR	21.176	23.327	24.183	24.366	24.372
	SSIM	0.537	0.647	0.680	0.685	0.685
	FSIM	0.755	0.801	0.817	0.821	0.821
Linear	PSNR	22.466	24.904	25.538	25.563	25.509
	SSIM	0.611	0.717	0.738	0.738	0.735
	FSIM	0.785	0.834	0.846	0.848	0.847
Cubic	PSNR	23.726	26.077	<b>26.287</b>	26.110	25.970
	SSIM	0.673	0.761	<b>0.765</b>	0.755	0.746
	FSIM	0.812	0.858	<b>0.863</b>	0.861	0.858

## V. CONCLUSIONS

In this paper, we propose to replace the Fourier transform by the framelet in the t-SVD framework. Then, we formulate the framelet representation of the tensor multi-rank and tensor nuclear norm. A low-rank tensor completion model is proposed by minimizing the framelet based tensor nuclear norm. We develop an ADMM based algorithm to solve this convex model with guaranteed convergence. We compare the performance of the proposed method with state-of-the-art



methods via numerical experiments on the magnetic resonance imaging data, videos, and multispectral images. Our method outperforms many state-of-the-art methods quantitatively and visually.

#### REFERENCES

- [1] M. Bertalmio, G. Sapiro, V. Caselles, and C. Ballester, “Image inpainting,” in *the Annual Conference on Computer Graphics and Interactive Techniques (SIGGRAPH)*, 2000, pp. 417–424. **1**
- [2] N. Komodakis, “Image completion using global optimization,” in *the IEEE Conference on Computer Vision and Pattern Recognition (CVPR)*, 2006, pp. 442–452.
- [3] T. Korah and C. Rasmussen, “Spatiotemporal inpainting for recovering texture maps of occluded building facades,” *IEEE Transactions on Image Processing*, vol. 16, no. 9, pp. 2262–2271, 2007.
- [4] J. Liu, P. Musialski, P. Wonka, and J. Ye, “Tensor completion for estimating missing values in visual data,” *IEEE Transactions on Pattern Analysis and Machine Intelligence*, vol. 35, no. 1, pp. 208–220, 2013. **1, 6, 7, 8**
- [5] R. Dian, L. Fang, and S. Li, “Hyperspectral image super-resolution via non-local sparse tensor factorization,” in *the IEEE Conference on Computer Vision and Pattern Recognition (CVPR)*. IEEE, 2017, pp. 3862–3871. **1**
- [6] S. Li, R. Dian, L. Fang, and J. M. Bioucas-Dias, “Fusing hyperspectral and multispectral images via coupled sparse tensor factorization,” *IEEE Transactions on Image Processing*, vol. 27, no. 8, pp. 4118–4130, 2018. **1**
- [7] J.-T. Sun, H.-J. Zeng, H. Liu, Y. Lu, and Z. Chen, “CubeSVD: a novel approach to personalized web search,” in *the International Conference on World Wide Web*, 2005, pp. 382–390. **1**
- [8] D. A. Lima and G. M. Oliveira, “A cellular automata ant memory model of foraging in a swarm of robots,” *Applied Mathematical Modelling*, vol. 47, pp. 551–572, 2017. **1**
- [9] T. G. Kolda, B. W. Bader, and J. P. Kenny, “Higher-order web link analysis using multilinear algebra,” in *the IEEE International Conference on Data Mining*, 2005, pp. 242–249. **1**
- [10] V. N. Varghees, M. S. Manikandan, and R. Gini, “Adaptive MRI image denoising using total-variation and local noise estimation,” in *the International Conference on Advances in Engineering, Science and Management (ICAESM)*, 2012, pp. 506–511. **1**
- [11] N. Kreimer and M. D. Sacchi, “A tensor higher-order singular value decomposition for prestack seismic data noise reduction and interpolation,” *Geophysics*, vol. 77, no. 3, pp. V113–V122, 2012. **1**
- [12] E. Candès and B. Recht, “Exact matrix completion via convex optimization,” *Communications of the ACM*, vol. 55, no. 6, pp. 111–119, 2012. **1**
- [13] Z. Song, D. Woodruff, and H. Zhang, “Sublinear time orthogonal tensor decomposition,” in *the Advances in Neural Information Processing Systems (NIPS)*, 2016, pp. 793–801. **1**
- [14] E. Acar, D. M. Dunlavy, T. G. Kolda, and M. Mørup, “Scalable tensor factorizations for incomplete data,” *Chemometrics and Intelligent Laboratory Systems*, vol. 106, no. 1, pp. 41–56, 2011. **1**
- [15] P. Tichavský, A.-H. Phan, and A. Cichocki, “Numerical cp decomposition of some difficult tensors,” *Journal of Computational and Applied Mathematics*, vol. 317, pp. 362–370, 2017. **1**
- [16] Y.-F. Li, K. Shang, and Z.-H. Huang, “Low tucker rank tensor recovery via admm based on exact and inexact iteratively reweighted algorithms,” *Journal of Computational and Applied Mathematics*, vol. 331, pp. 64–81, 2018. **1**
- [17] X. Li, M. K. Ng, G. Cong, Y. Ye, and Q. Wu, “MR-NTD: manifold regularization nonnegative tucker decomposition for tensor data dimension reduction and representation,” *IEEE transactions on neural networks and learning systems*, vol. 28, no. 8, pp. 1787–1800, 2017. **1**
- [18] S. Gandy, B. Recht, and I. Yamada, “Tensor completion and low-n-rank tensor recovery via convex optimization,” *Inverse Problems*, vol. 27, no. 2, p. 025010, 2011. **1**
- [19] C. J. Hillar and L.-H. Lim, “Most tensor problems are NP-hard,” *Journal of the ACM (JACM)*, vol. 60, no. 6, p. 45, 2013. **1**
- [20] K. Braman, “Third-order tensors as linear operators on a space of matrices,” *Linear Algebra and its Applications*, vol. 433, no. 7, pp. 1241–1253, 2010. **1**
- [21] M. E. Kilmer and C. D. Martin, “Factorization strategies for third-order tensors,” *Linear Algebra and its Applications*, vol. 435, no. 3, pp. 641–658, 2011. **1, 2, 3**
- [22] M. E. Kilmer, K. Braman, N. Hao, and R. C. Hoover, “Third-order tensors as operators on matrices: A theoretical and computational framework with applications in imaging,” *SIAM Journal on Matrix Analysis and Applications*, vol. 34, no. 1, pp. 148–172, 2013. **1, 2, 3**
- [23] C. D. Martin, R. Shafer, and B. LaRue, “An order-p tensor factorization with applications in imaging,” *SIAM Journal on Scientific Computing*, vol. 35, no. 1, pp. A474–A490, 2013. **1**
- [24] Y.-B. Zheng, T.-Z. Huang, X.-L. Zhao, T.-X. Jiang, T.-Y. Ji, and T.-H. Ma, “Tensor n-tubal rank and its convex relaxation for low-rank tensor recovery,” *arXiv preprint arXiv:1812.00688*, 2018. **1**
- [25] E. Kernfeld, M. Kilmer, and S. Aeron, “Tensor–tensor products with invertible linear transforms,” *Linear Algebra and its Applications*, vol. 485, pp. 545–570, 2015. **1**
- [26] Z. Zhang, G. Ely, S. Aeron, N. Hao, and M. Kilmer, “Novel methods for multilinear data completion and de-noising based on tensor-SVD,” in *the IEEE Conference on Computer Vision and Pattern Recognition (CVPR)*, 2014, pp. 3842–3849. **1, 2, 3**
- [27] C. Lu, J. Feng, Y. Chen, W. Liu, Z. Lin, and S. Yan, “Tensor robust principal component analysis: Exact recovery of corrupted low-rank tensors via convex optimization,” in *Proceedings of the IEEE Conference on Computer Vision and Pattern Recognition*, 2016, pp. 5249–5257. **1, 2**
- [28] J. Q. Jiang and M. K. Ng, “Exact tensor completion from sparsely corrupted observations via convex optimization,” *arXiv preprint arXiv:1708.00601*, 2017. **2**
- [29] C. Lu, J. Feng, Y. Chen, W. Liu, Z. Lin, and S. Yan, “Tensor robust principal component analysis with a new tensor nuclear norm,” *IEEE Transactions on Pattern Analysis and Machine Intelligence (TPAMI)*, 2018.
- [30] W. Hu, D. Tao, W. Zhang, Y. Xie, and Y. Yang, “The twist tensor nuclear norm for video completion,” *IEEE transactions on neural networks and learning systems*, vol. 28, no. 12, pp. 2961–2973, 2017. **2, 6, 7, 8**
- [31] W.-H. Xu, X.-L. Zhao, and M. K. Ng, “A fast algorithm for cosine transform based tensor singular value decomposition,” *Preprint*. **2**
- [32] C. Lu, X. Peng, and Y. Wei, “Low-rank tensor completion with a new tensor nuclear norm induced by invertible linear transforms,” in *Proceedings of the IEEE Conference on Computer Vision and Pattern Recognition*, 2019, pp. 5996–6004. **2**
- [33] G. Song, M. K. Ng, and X. Zhang, “Robust tensor completion using transformed tensor SVD,” *arXiv preprint arXiv:1907.01113*, 2019. **2**
- [34] J.-F. Cai, R. H. Chan, and Z. Shen, “A framelet-based image inpainting algorithm,” *Applied and Computational Harmonic Analysis*, vol. 24, no. 2, pp. 131–149, 2008. **2, 4**
- [35] S. Boyd, N. Parikh, E. Chu, B. Peleato, J. Eckstein *et al.*, “Distributed optimization and statistical learning via the alternating direction method of multipliers,” *Foundations and Trends® in Machine learning*, vol. 3, no. 1, pp. 1–122, 2011. **2, 5**
- [36] T.-X. Jiang, T.-Z. Huang, X.-L. Zhao, T.-Y. Ji, and L.-J. Deng, “Matrix factorization for low-rank tensor completion using framelet prior,” *Information Sciences*, vol. 436–437, pp. 403–

- 417, 2017. 4
- [37] A. Ron and Z. Shen, “Affine systems in $l_2$  (rd): the analysis of the analysis operator,” *Journal of Functional Analysis*, vol. 148, no. 2, pp. 408–447, 1997. 4
- [38] J.-F. Cai, E. J. Candès, and Z. Shen, “A singular value thresholding algorithm for matrix completion,” *SIAM Journal on Optimization*, vol. 20, no. 4, pp. 1956–1982, 2010. 5
- [39] Z. Wang, A. C. Bovik, H. R. Sheikh, and E. P. Simoncelli, “Image quality assessment: from error visibility to structural similarity,” *IEEE Transactions on Image Processing*, vol. 13, no. 4, pp. 600–612, 2004. 5
- [40] L. Zhang, L. Zhang, X. Mou, and D. Zhang, “FSIM: A feature similarity index for image quality assessment,” *IEEE transactions on Image Processing*, vol. 20, no. 8, pp. 2378–2386, 2011. 5
- [41] X. Li, Y. Ye, and X. Xu, “Low-rank tensor completion with total variation for visual data inpainting,” in *Thirty-First AAAI Conference on Artificial Intelligence*, 2017. 6, 7, 8
- [42] Z. Zhang and S. Aeron, “Exact tensor completion using t-SVD,” *IEEE Transactions on Signal Processing*, vol. 65, no. 6, pp. 1511–1526, 2017. 6, 7, 8
- [43] T.-X. Jiang, T.-Z. Huang, X.-L. Zhao, and L.-J. Deng, “A novel nonconvex approach to recover the low-tubal-rank tensor data: when t-svd meets pssv,” *arXiv preprint arXiv:1712.05870*, 2017. 6, 7, 8
- [44] F. Yasuma, T. Mitsunaga, D. Iso, and S. K. Nayar, “Generalized assorted pixel camera: postcapture control of resolution, dynamic range, and spectrum,” *IEEE transactions on image processing*, vol. 19, no. 9, pp. 2241–2253, 2010. 7
- [45] Q. Xie, Q. Zhao, D. Meng, Z. Xu, S. Gu, W. Zuo, and L. Zhang, “Multispectral images denoising by intrinsic tensor sparsity regularization,” in *Proceedings of the IEEE Conference on Computer Vision and Pattern Recognition*, 2016, pp. 1692–1700. 7